



# Template bacteria-free fabrication of surface imprinted polymer-based biosensor for *E. coli* detection using photolithographic mimics: Hacking bacterial adhesion

Dua Özsoylu<sup>a</sup>, Fereshteh Aliazizi<sup>b</sup>, Patrick Wagner<sup>b</sup>, Michael J. Schöning<sup>a, c, \*</sup>

<sup>a</sup> Institute of Nano- and Biotechnologies (INB), Aachen University of Applied Sciences, Campus Jülich, 52428, Jülich, Germany

<sup>b</sup> Department of Physics and Astronomy, Laboratory for Soft Matter and Biophysics, KU Leuven, B-3001, Leuven, Belgium

<sup>c</sup> Institute of Biological Information Processing (IBI-3), Research Centre Jülich GmbH, 52425, Jülich, Germany

## ARTICLE INFO

### Keywords:

Surface imprinted polymer  
*E. coli* detection  
 Photolithographic mimics  
 Master stamp  
 Quartz crystal microbalance  
 Impedance spectroscopy

## ABSTRACT

As one class of molecular imprinted polymers (MIPs), surface imprinted polymer (SIP)-based biosensors show great potential in direct whole-bacteria detection. Micro-contact imprinting, that involves stamping the template bacteria immobilized on a substrate into a pre-polymerized polymer matrix, is the most straightforward and prominent method to obtain SIP-based biosensors. However, the major drawbacks of the method arise from the requirement for fresh template bacteria and often non-reproducible bacteria distribution on the stamp substrate. Herein, we developed a positive master stamp containing photolithographic mimics of the template bacteria (*E. coli*) enabling reproducible fabrication of biomimetic SIP-based biosensors without the need for the “real” bacteria cells. By using atomic force and scanning electron microscopy imaging techniques, respectively, the *E. coli*-capturing ability of the SIP samples was tested, and compared with non-imprinted polymer (NIP)-based samples and control SIP samples, in which the cavity geometry does not match with *E. coli* cells. It was revealed that the presence of the biomimetic *E. coli* imprints with a specifically designed geometry increases the sensor *E. coli*-capturing ability by an “imprinting factor” of about 3. These findings show the importance of geometry-guided physical recognition in bacterial detection using SIP-based biosensors. In addition, this imprinting strategy was employed to interdigitated electrodes and QCM (quartz crystal microbalance) chips. *E. coli* detection performance of the sensors was demonstrated with electrochemical impedance spectroscopy (EIS) and QCM measurements with dissipation monitoring technique (QCM-D).

## 1. Introduction

In today's globalized world with a highly mobile, interconnected and interdependent nature, diseases caused by pathogenic bacteria spread rapidly, and this results in a serious global threat to modern health care as well as environment and food safety (Park, 2018). As an example, according to the estimations of the World Health Organization (WHO), 600 million people every year become ill after consuming contaminated food (World Health Organization, 2022), where the majority of them are related to pathogenic bacteria (World Health Organization, 2015), and 420,000 people die every year due to the consumption of contaminated food (World Health Organization, 2022). To combat this global threat, the development of advanced diagnostic methods for the detection, identification and monitoring of the pathogenic bacteria is crucial.

Traditionally, bacterial culture-based techniques and biochemical staining methods are considered the clinical gold standard for identifying bacterial pathogens (Park, 2018). However, as these methods usually rely on morphological and biochemical characterizations, they may not easily detect some bacteria strains (Abayasekara et al., 2017) as well as they require long testing times (up to several days) from sampling to final assessment (Park, 2018; Filby et al., 2020). Other methods, such as polymerase chain reaction (PCR) (Law et al., 2015), enzyme-linked immunosorbent assays (ELISA) (Zhao et al., 2020), Raman spectroscopy (Pahlow et al., 2015), or flow cytometry (Velican et al., 2020) are also common techniques for pathogenic bacteria detection; however, these methods are usually costly, time-consuming and incompatible with field testing since they require sample pre-/multistep-processing, trained personnel and centralized laboratories

\* Corresponding author. Institute of Nano- and Biotechnologies (INB), Aachen University of Applied Sciences, Campus Jülich, 52428, Jülich, Germany.  
 E-mail address: [schoening@fh-aachen.de](mailto:schoening@fh-aachen.de) (M.J. Schöning).

<https://doi.org/10.1016/j.bios.2024.116491>

Received 13 April 2024; Received in revised form 5 June 2024; Accepted 7 June 2024

Available online 13 June 2024

0956-5663/© 2024 The Authors. Published by Elsevier B.V. This is an open access article under the CC BY-NC license (<http://creativecommons.org/licenses/by-nc/4.0/>).

(Castle et al., 2021; Mazur et al., 2023). The sensing methods allowing direct whole bacteria detection are a growing trend because this minimizes the requirement of sophisticated/time-consuming sample preparation steps (e.g., deoxyribonucleic acid (DNA) isolation and purification), and therefore, facilitates field-deployable applications (e.g., point-of-care diagnostic systems) (Park, 2018; Cornelis et al., 2019; Castle et al., 2021). Thus, biosensors incorporated with specific bio-recognition elements such as aptamers, antibodies or imprinted polymers are the most promising options to ensure direct whole bacteria detection (Park, 2018; Zaracee et al., 2020; Castle et al., 2021). On the other hand, compared with their counterparts, imprinted polymer-based biosensors received widespread attention due to their robustness, cost-effectiveness and long shelf life (Uzun and Turner, 2016; Golabi et al., 2017; Yang et al., 2018; Cornelis et al., 2019; Kavand et al., 2019; Jamal et al., 2020; Givanoudi et al., 2021).

The molecular imprinting process commonly consists of copolymerization of functional monomers and targeted ligands (e.g., the template bacteria or template molecule) with a suitable cross-linker. After the polymerization, the template is removed to form specific binding cavities ("artificial receptors") that are complementary in geometry (shape and size) and most importantly, functionality to the template (Chen et al., 2016). The whole-bacteria-imprinting method is the most preferred strategy to create bacteria-specific binding cavities (recognition sites) on polymeric matrices. As a soft lithography method, micro-contact imprinting that involves stamping of the template bacteria immobilized on a substrate (usually polydimethylsiloxane (PDMS)) into the pre-polymerized polymer matrix containing functional monomers and cross-linker is the most straightforward and efficient method to obtain bacteria-imprinted polymers (Chen et al., 2016; Eersels et al., 2016; Pan et al., 2018; Piletsky et al., 2020; Yadav et al., 2022). The stamping is performed on the sensor surface (e.g., planar electrodes, interdigitated electrodes or quartz crystal microbalance (QCM) chips) coated with a pre-polymerized polymer matrix (e.g., polyurethane, photopolymers) to obtain surface imprinted polymer (SIP)-based sensor chips. Thereafter, the sensor surface consists of bacteria-imprinted cavities with complementary sizes and shapes of the target bacteria, which is crucial for geometry-dependent physical recognition. On the other hand, bacterial extracellular components such as surface receptors, lipopolysaccharides or membrane proteins also leave their imprints on the bacteria-imprinted cavities, which is important for chemical recognition of the target bacteria. The synergistic effect of both physical and chemical recognition favors high affinity to target bacteria, the corresponding realization of better detection ability (Chen et al., 2016; Pan et al., 2018; Yongabi et al., 2018; Yadav et al., 2022; Caldara et al., 2023).

Although micro-contact imprinting is a versatile and efficient method for the development of SIP-based sensors with bacteria imprints, hence showing great potential in direct whole-bacteria detection (Latif et al., 2014; Yilmaz et al., 2015; Steen Redeker et al., 2017; Idil et al., 2017, 2021; Poller et al., 2017; Cornelis et al., 2019; Stilman et al., 2022; Iakimova et al., 2024), the method still fails to address some fundamental challenges. The major drawback of the method arises from the heterogeneous nature of the prepared bacterial stamps. It is almost impossible to prepare a stamp whose bacteria are distributed on its surface always with the same level of surface coverage (e.g., controlled areal density and distribution). Due to this irreproducibility and irregularity, each stamp forms different cavity distributions with different imprint densities on SIP layers, which cause run-to-run variations during measurements (Caldara et al., 2023). Therefore, standardization should be ensured if the surface imprinting technology is up-scaled to serial production. As one of the other drawbacks, the method requires the cultivation and preparation of the template bacteria to fabricate a sensor chip, which is a laborious and time-consuming process that also demands special laboratories and experienced staff. In addition, when it comes to sensitive, expensive or dangerous bacteria species, special precautions must be taken, for example, to avoid the risk of template

leakage (Chen et al., 2016). Finally, it was reported that bacteria cells flattened due to the compression in the micro-contact imprinting process. This causes cavities that are not in the same shape as the original template cell in solution, which might influence the affinity of the cells towards the cavities (Werner et al., 2022). From that point of view, a novel micro-contact imprinting technology that does not require template bacteria and ensures reproducible and standard bacterial imprints (cavities) is highly desirable.

In this work, we present a SIP-based biosensor for the direct detection of whole bacteria by utilizing a positive master stamp containing photolithographic mimics of the template bacteria (*E. coli* as a model organism). By micro-contact imprinting method using the developed master stamp, SIP layers with biomimetic structural analogues of the *E. coli* imprints in a desired areal density, distribution and orientation were achieved. The *E. coli*-capturing ability of the developed SIP layers was studied by microscopic methods, such as atomic force microscopy (AFM) and scanning electron microscopy (SEM). The important findings have been revealed regarding the contribution of geometry-dependent physical recognition in the SIP-based bacteria detection biosensor. The SIP layer was employed on two different types of sensor chips: customized interdigitated electrodes (IDE) structures and QCM electrodes. As a proof-of-concept study, the bacteria detection feasibility of the developed sensor chips was demonstrated using electrochemical impedance spectroscopy (EIS) and quartz crystal microbalance with dissipation monitoring technique (QCM-D). This work represents the first step towards "template bacteria-free" fabrication of SIP layers with high cavity density.

## 2. Material and methods

### 2.1. Fabrication of the interdigitated electrodes

The electrodes were designed using CAD software (KLayout). The finger width, spacing between the fingers, length of the fingers and total number of the fingers were adjusted to be 10  $\mu\text{m}$ , 5  $\mu\text{m}$ , 8 mm and 334, respectively. Direct laser writing lithography was used for the fabrication of the electrode patterns on the sensor chip. For this, an image reversal photoresist (AZ 5214E [JP], diluted 1:0.476, Microchemicals GmbH, Germany) was first spin-coated (4000 RPM, 30 s) on a glass wafer (0.5 mm thick, Borofloat 33, SIEGERT WAFER GmbH, Germany) followed by a soft bake at 105  $^{\circ}\text{C}$  for 1.5 min. Laser writing was performed with a 405 nm laser source of a direct laser writer device (PicoMaster 150, Raith GmbH) by applying an exposure energy of 35.96  $\text{mJ}/\text{cm}^2$  (spot size: 550 nm, step resolution: 275 nm). Afterwards, a reversal-bake at 120  $^{\circ}\text{C}$  was applied and followed by flood exposure at 900  $\text{mJ}/\text{cm}^2$ . Then, structures were achieved after developing with tetramethyl-ammonium hydroxide (TMAH, 2.38% in  $\text{H}_2\text{O}$ , AZ 726 MIF, Microchemicals GmbH, Germany) for 1 min. The physical vapor deposition technique was applied for the deposition of first titanium (10 nm) and then, platinum (100 nm) on the wafer. After the metallization, dimethyl sulfoxide (Micro D350, Microchemicals GmbH, Germany) is used as a lift-off medium for 2 h at 60  $^{\circ}\text{C}$ . After the lift-off, the wafer was diced to obtain the sensor chips with a size of 2 cm  $\times$  2 cm.

### 2.2. Fabrication of master mold and positive master stamp

Fig. 1a demonstrates the major fabrication steps of the SIP-based sensor chips. In brief, the fabrication steps are (from left to right) i) photolithographic patterning of a photoresist to achieve a master mold with biomimetic structural analogues of *E. coli* imprints, ii) pattern transferring by molding (soft-lithography) to obtain a PDMS-based positive master stamp with biomimetic *E. coli*-like structures (protrusions), and iii) imprinting with the master stamp on the sensor surface to obtain biomimetic structural analogues of *E. coli* imprints (exemplary sketched for IDEs).

For the master mold, the geometry of the patterns (cavities) was

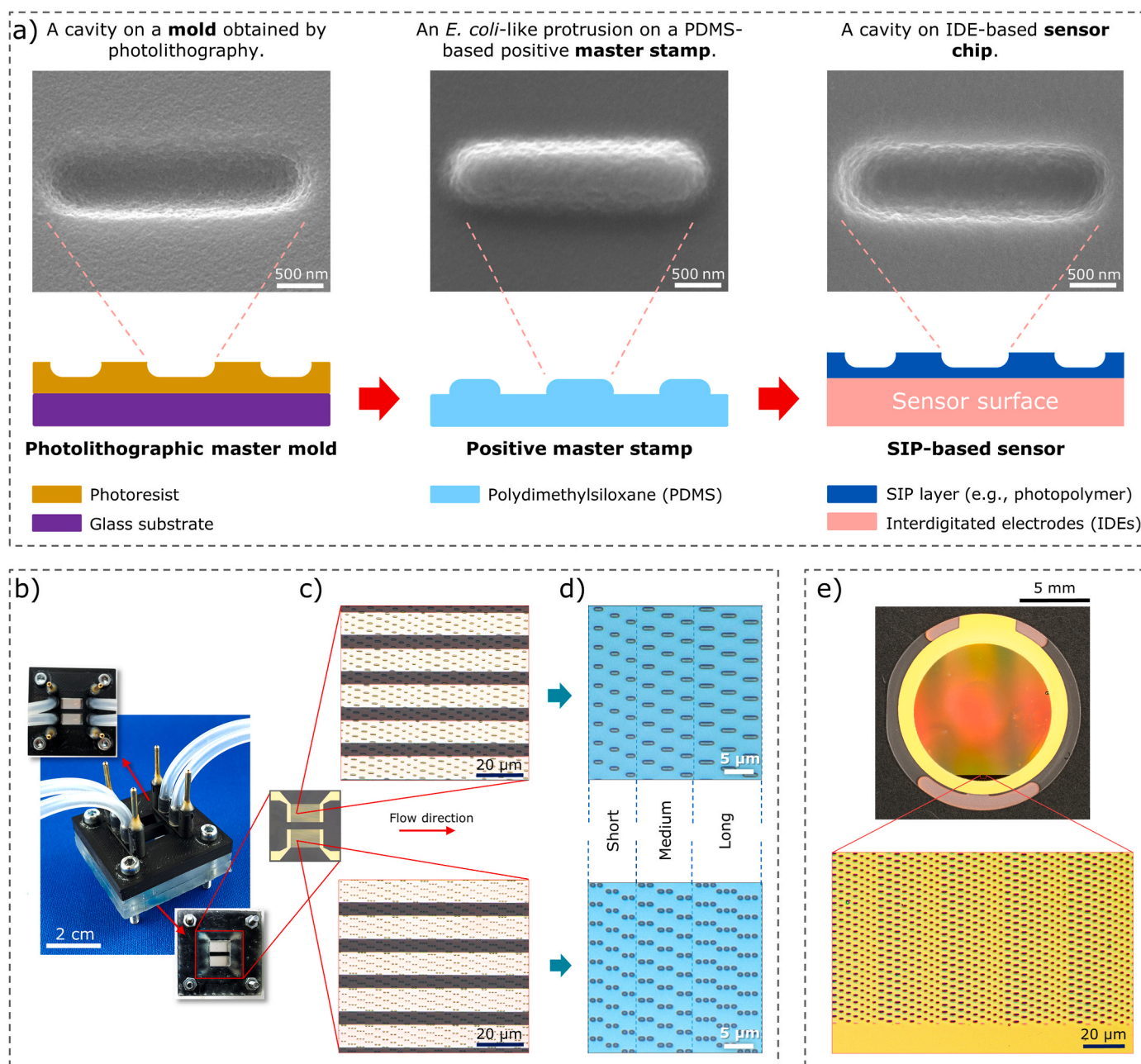


**Fig. 1.** Template bacteria-free fabricated surface imprinted polymer-based biosensor for *E. coli* detection. a) Fabrication process for polymer imprinting (schematically, bottom row) and corresponding SEM images (top row): photolithographic patterning of photoresist to achieve a master mold with biomimetic structural analogues of *E. coli* imprints, pattern transfer by molding (soft-lithography) to obtain a PDMS-based master stamp, and imprinting with the master stamp on the sensor chip surface (from left to right). b) Images of the electrochemical impedance spectroscopy (EIS)-based sensing set-up with flow cell containing two parallel channels. c) Digital microscopy images of interdigitated electrodes (IDEs) coated by the SIP layer composed of a photopolymer resin. The zoom-in digital microscopy images (d) depict two different SIP types for differential analysis: the *E. coli* SIP (upper image) and the control SIP (lower image). e) Images of a quartz crystal microbalance (QCM) sensor chip coated by the *E. coli* SIP layer.

designed by a CAD software (KLayout) according to the characteristics of the rod-shaped *E. coli* cells, reported in the literature (Reshes et al., 2008). Hence, the width of the cavities was kept constant at 0.8  $\mu\text{m}$  while the length was designed in three different sizes: 2.6  $\mu\text{m}$  (long), 2.1  $\mu\text{m}$  (medium), and 1.6  $\mu\text{m}$  (short) to explore a wider range of possibilities to capture the bacterial cells as they are different in size depending on their age and living conditions (Reshes et al., 2008). This design was named “*E. coli* SIP” (see upper images in Fig. 1c and d and lower image in Fig. 1e). Another pattern has been designed in a way that the cavity geometry does not match with *E. coli* target bacteria while it provides comparability to explore the effect of cavity geometry on cell capturing:

This was achieved by dividing the former cavities “short” and “medium” by a factor of two, and “long” by a factor of three (see lower images in Fig. 1c and d), and this design was called as “control SIP”. The areal density of the cavities (see upper images in Fig. 1c and d) was defined as  $10^7$  cavities/ $\text{cm}^2$ . To fabricate the master mold (Fig. 1a, left), similar photolithographic fabrication steps, as mentioned in Section 2.1, have been followed with slight modifications. The same photoresist (AZ 5214E [JP]) was employed, but this time in the positive mode. To achieve *E. coli*-like cavities with a curved geometry only on the surface of the photoresist without involving the flat glass substrate underneath, the laser exposure energy was optimized by testing different energy

values. It was found out that an exposure energy of 40 mJ/cm<sup>2</sup> gives an ideal outcome in terms of geometrical similarity with *E. coli*. After the exposure, the development was performed without reversal-bake. To enhance the adhesion and chemical stability of the obtained master mold, it underwent a flood exposure at 200 mJ/cm<sup>2</sup>, followed by post-bake at 120 °C for 3 min.

Transferring the patterns by molding (see Fig. 1a, middle) was performed by soft-lithography using a two-component polydimethylsiloxane elastomer (SYLGARD 184, Dow, USA). For this, PDMS was prepared at a standard mixing ratio (10:1, vacuum degassed) according to the instructions of the manufacturer. The mixture was then poured on the mold inserted into a glass Petri dish and degassed again under vacuum to prevent any possible air bubbles from being trapped in the cavities. The curing of the elastomer was performed at 100 °C for 35 min using a hotplate. After curing, the positive master stamp was separated from the mold and cut to the desired size with a razor blade.

### 2.3. Surface imprinting

Surface imprinting (Fig. 1a, right) with the master stamp was performed on the IDE-based sensor chips (see Section 2.1) as well as on the QCM sensor chips (QXS 301 Gold, Biolin Scientific AB, Sweden). For this, a commercially available photopolymer resin (AZ 5214E [JP], Microchemicals GmbH) based on diazonaphthoquinone sulfonic acid ester and cresol novolak resin was further diluted with propylene-glycol-mono-methylether-acetate (dilution ratio 1:0.476) to obtain ca. 600 nm thick SIP layers. The resin was spin-coated on the sensor surface at 4000 RPM for 30 s after cleaning the surface with acetone and isopropanol in an ultrasonic bath for 10 min. Right after the spin-coating process, stamping was performed by pressing the master stamp onto the coated sensor surface, followed by soft bake at 105 °C for 1.5 min. After the soft bake, the stamp was peeled off and the patterns were obtained on the sensor surface. To enhance the adhesion and chemical stability, post-processing has been utilized with a flood exposure (250 mJ/cm<sup>2</sup>) and post-bake (120 °C for 3 min). For non-imprinted polymer (NIP) samples, the same procedure was followed except for the usage of stamp samples; instead, a flat and non-patterned PDMS sample was employed.

### 2.4. Characterizations of the obtained SIPs

A digital microscope (VHX-7000, Keyence, USA) was used for the general characterization and quality control of the imprinting process of the obtained patterns (e.g., Fig. 1c,d,e) while SEM was utilized to study the structures in more detail. The SEM images have been recorded using an SEM device (JSM-7800F, Jeol GmbH, Germany) after sputtering of a platinum-palladium layer (around 5–10 nm thick) on the samples (e.g., Fig. 1a, upper images). AFM was applied to determine the topography of the patterned surfaces. The samples were scanned in non-contact mode using a silicon-based cantilever (ARROW-NCR-20, Switzerland) assembled on an AFM device (BioMat Workstation, JPK Instruments, Germany). An electrokinetic analyzer (SurPASS 3, Anton Paar GmbH, Austria) was used to explore the Zeta potential of the SIP layer. Zeta potentials of the samples were calculated from the streaming potential measurements, where 1 mM KCl solution was used as an analyte solution. In addition, an optical drop shape analyzer (DSA30E, Krüss, Germany) was used for evaluating surface wettability by means of contact angle measurement of a sessile drop (2 µL of ultrapure water), dosed onto the sensor chips. The surface free energy of the samples was explored by measuring the contact angle of a sessile drop of 2 µL of ultrapure water and 2 µL of diiodomethane. The surface energy of the samples was calculated according to Owens, Wendt, Rabel and Kaelble's (OWRK) method (Owens and Wendt, 1969) using the device's software.

### 2.5. Bacteria cultivation and preparation

*E. coli*-K12 bacteria cells (DSM498, DSMZ GmbH, Germany) from several colonies in the same Petri dish were inoculated into 10 mL of Luria-Bertani (LB) medium and the mixture was incubated overnight at 37 °C in a shaking incubator to allow the bacteria reach late log phase. The culture was then centrifuged at 6000 RPM for 5 min and resuspended in sterile phosphate-buffered saline (PBS) solution (pH 7.4) after removing the supernatant. This procedure was repeated three times to properly wash the cells and remove residues of the culture medium. The optical density of the bacteria solution was recorded at 600 nm using a spectrometer in addition to counting the cells using a hemocytometer to determine the number of cells obtained. The bacteria solution was diluted using the PBS solution to achieve the desired concentrations (from 10<sup>4</sup> cells/mL to 10<sup>9</sup> cells/mL in PBS) required in the following experiments.

### 2.6. Analysis of cell capturing

For differential analysis of *E. coli* capturing performance of the control SIP and *E. coli* SIP layers, a parallel channel flow cell (Fig. 1b) was used to introduce the bacteria solutions to the sensor chip. The components of the flow cell were designed with a 3D CAD Software (Autodesk Inventor). Fig. S1 (Supplementary Information) demonstrates the design details of the components (from top to bottom): the upper layer that holds electrical contacts (spring-loaded pins) and tube connections, the middle layer that defines the channels of the flow cell on the sensor surface, and the bottom layer that holds the sensor chip. The PDMS-based middle layer was fabricated using a 3D-printed mold (Fig. S1, middle image). The final view of the flow cell, housing the inserted sensor chip, is shown in Fig. 1b.

*E. coli*-K12 bacteria in PBS (10<sup>8</sup> cells/mL) were flushed into the channels of the flow cell, then, the sensor surface was exposed to the bacteria cells for either 10 min or 20 min under static conditions (no-flow) at room temperature (around 21 °C). These two incubation durations (10 min and 20 min) were selected to observe the effect of incubation time on *E. coli* capturing effectiveness of the SIP layers, because those incubation times are typically discussed in literature for conventional MIP-based sensors (see e.g., (Yilmaz et al., 2015; Idil et al., 2017; Cornelis et al., 2019; Arreguin-Campos et al., 2021; Idil et al., 2021; Givanoudi et al., 2021; Arreguin-Campos et al., 2022)). Afterwards, the channels were rinsed with PBS solution with a flow rate of 1.2 mL/min for 5 min. A cell fixation solution (2.5% glutaraldehyde in PBS) was added into the channels and incubated at room temperature (21 °C) overnight to fixate the cells for AFM and SEM analysis. To exchange the fixation solution, the channels of flow cell were rinsed with ultrapure water, and then the channels were dried by nitrogen gas. The sensor chip was removed from the flow cell for microscopic examinations. AFM and SEM analysis were performed as described in Section 2.4. The number of cells that stayed on the surface was counted from SEM images by using the software ImageJ (Schneider et al., 2012). The *E. coli* cells inside the cavities and outside the cavities were counted separately to examine the cell-capturing ability of not only whole surfaces but also individual cavities.

### 2.7. Signal measurements

To evaluate the feasibility of *E. coli* detection with the developed sensor chips, two different sensing methods have been employed: electrochemical impedance spectroscopy (EIS) and quartz crystal microbalance with dissipation monitoring (QCM-D). For EIS measurements, a sensor chip with *E. coli* SIP was mounted into the flow cell as mentioned in Section 2.6. The *E. coli*-K12 cells were introduced to the channels of the flow cell in different concentrations (from 10<sup>4</sup> cells/mL to 10<sup>9</sup> cells/mL in PBS) after recording a baseline signal using sterile PBS solution. For each cell concentration, the bacteria solution was incubated for 20

min under static conditions (no-flow) at room temperature (21 °C), followed by washing with PBS solution to remove unattached cells with a flow rate of 20  $\mu\text{L}/\text{s}$  for 2 min. EIS signal recordings were performed by sweeping the frequency from 100 mHz to 5 MHz at an alternating current (AC) voltage amplitude of 20 mV (under open-circuit conditions) after filling the channels with 10 mM  $\text{Fe}(\text{CN})_6^{3-}/\text{Fe}(\text{CN})_6^{4-}$  in PBS as a redox probe. After the measurement of the cell concentrations, sodium dodecyl sulfate (SDS) solution (2% in ultrapure water) was flushed in the channels of the flow cell with a flow rate of 1.2 mL/min for 5 min to clean the sensor surface from cells for evaluating the signal recovery. Hence, the final measurement was performed after filling the channels with the redox probe.

For QCM-D measurements, the sensor chip (Fig. 1e) was inserted into the flow chamber (QFM 401, QSense® Flow module, Biolin Scientific AB, Sweden) of a QCM device (Q-Sense E4, Biolin Scientific AB, Sweden). PBS solution was introduced to the channel of the flow module and the measurements were performed after allowing the system to equilibrate and obtain a stable baseline. The frequency shift ( $\Delta f$ ) and energy

dissipation ( $\Delta D$ ) were monitored corresponding to the different concentrations (from  $10^4$  cells/mL to  $10^9$  cells/mL in PBS) of *E. coli*-K12 cells introduced onto the sensor surface with a flow rate of 100  $\mu\text{L}/\text{min}$  for 20 min at 19 °C. Then, the measurement was continued under static conditions (no-flow) for 30 min. Afterwards, the same timing procedure was applied with PBS solution (no cells) to wash the surface with a flow rate of 50  $\mu\text{L}/\text{min}$ . At the end, cleaning the surface from the cells was performed using SDS solution, as mentioned above. The final measurement was performed after filling the channel with PBS solution.

### 3. Results and discussion

#### 3.1. SIP layer characteristics

To achieve reproducible measurement results, it is important to fabricate a SIP layer on a sensor surface, ideally without any defect on the layer and its cavities. In addition, the fabrication outcome should provide cavities whose geometry matches that of the target bacteria

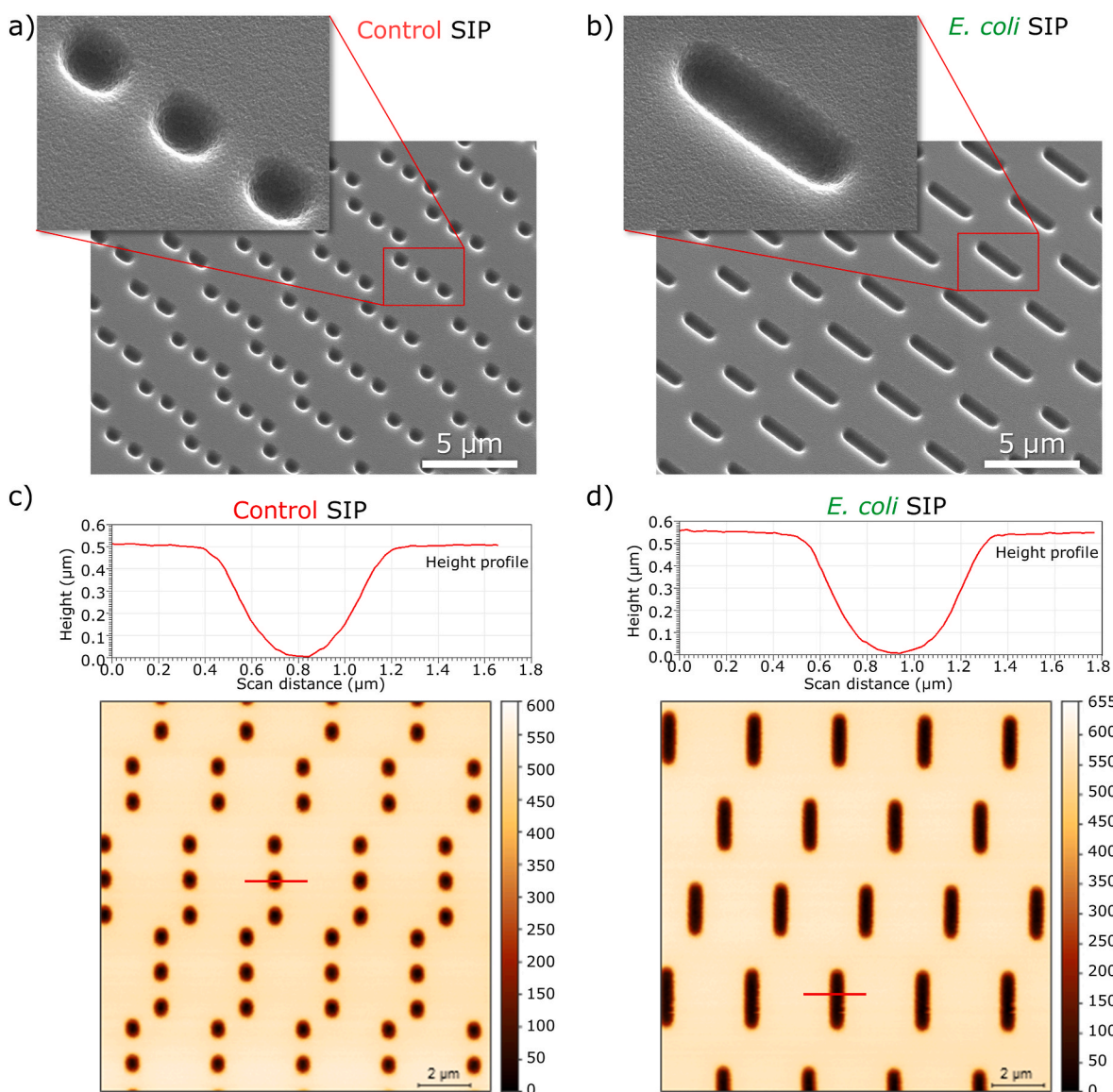


**Fig. 2.** Physical characteristics of the SIP layers. a)-b) SEM images of the SIP layers showing the cavities on the sensor surface. The images demonstrate two types of the SIP layer for differential analysis: a) Control SIP, in which the cavity geometry does not match with *E. coli* cells (control samples), and b) *E. coli* SIP containing the biomimetic *E. coli* cavities as structural analogues of the real *E. coli* imprints. c)-d) 2-D AFM images along with the line profiles of the SIP layers show surface topography and the geometry of the cavities. The images with line profiles correspond to two types of the SIP layer: c) control SIP, and d) *E. coli* SIP. The height profiles (on top) correspond to the red line on the 2-D images below drawn over a row of the cavities, showing their cross-sectional geometries.

(here, rod-shaped *E. coli*-K12). Fig. 2a and b demonstrate exemplary SEM images of the sensor chip surfaces including control SIP and *E. coli* SIP. The images indicate a homogeneous and defect-free transfer of the photolithographic patterns to the sensor surface. More importantly, a curved geometry, which is a necessity for mimicking rod-shaped *E. coli*, could be successfully achieved. To show these surface features in even more details, additional SEM images are provided in Fig. S2 (Supplementary Information).

AFM imaging was utilized to analyze further details of the obtained SIP layers such as the depth and 3-D geometry of the cavities. Fig. 2c and d show representative AFM topography images of the sensor chip surfaces. Corresponding to the SEM images in Fig. 2a and b, the homogeneous and defect-free imprinting on the sensor surface was also confirmed by AFM imaging. The line profiles above the AFM images indicate the depth of the cavities (around 500 nm for the control SIP and around 530 nm for the *E. coli* SIP) while the length was measured as around 2.6  $\mu\text{m}$  for long cavities, 2.1  $\mu\text{m}$  for medium cavities, and 1.6  $\mu\text{m}$  for short cavities. These characteristics of the SIP layers indicate that the biomimetic *E. coli* structures (protrusions) on the master stamp show high geometric similarity with the real *E. coli* bacteria (Reshes et al., 2008), and the achieved biomimetic imprints on the sensor surface provide high structural similarity with that of the real *E. coli* imprints reported in the literature (Cornelis et al., 2019; Werner et al., 2022; Stilman et al., 2022). In addition, 3-D topography images of the AFM measurements with different view perspectives are available in Fig. S3 (Supplementary Information).

One of the most important goals for fabricating SIP-based sensors is to form imprints (cavities) with an as high as possible areal density (Iakimova et al., 2024). By utilizing the pioneering “Dickert’s imprinting” approach (representing the established SIP fabrication method), our group could previously achieve an imprint density of  $6.5 \times 10^6$  imprints per  $\text{cm}^2$  after several optimization studies using *E. coli* bacteria (Cornelis et al., 2019). The difficulty in reaching higher imprint densities with uniform distribution arises from overlapping or cluster formation of bacteria due to the aggregation of *E. coli* cells when they are applied to the stamp surface in higher concentrations, which results in a poor signal response (Iakimova et al., 2024). Remarkably, in the current work, we achieved  $10^7$  imprints per  $\text{cm}^2$  in a standard/reproducible way (thanks to the developed master stamp) without using any template bacteria. Moreover, the imprint density can further be increased as there is still some remaining flat area between the cavities on the *E. coli* SIP surface where more cavities can later be located.

It is well known that the bacterial adhesion, and consequently the sensor capturing ability, is also strongly affected by the physico-chemical properties of the surfaces (Zheng et al., 2021). Therefore, the surface charge of the fabricated sensor chips (in fact, the SIP layer consists of a photopolymer resin) was evaluated with an electrokinetic analyzer. Fig. S4a (Supplementary Information) shows the surface zeta potential (indicating the surface charge properties) as a function of analyte pH values. The results indicate that the sensor surface has a net negative charge, e.g., around  $-85$  mV at pH 7.4, where measurements are often performed at this physiological condition. Under the conditions we used in our study (PBS buffer), the *E. coli* bacteria will have a net negative charge as well (Li and McLandsborough, 1999), resulting in repulsive electrostatic interactions between the SIP surface and the bacteria. Nevertheless, it is also known that such interactions are sensitive to the solution’s ionic strength, and the *E. coli* adhesion can occur regardless of the surface charge when a high ionic strength solution (such as the PBS buffer in this work) is used for exposing the cells on the sensor surface (Walker et al., 2005; Zheng et al., 2021; Yongabi et al., 2021). This hypothesis is confirmed by a recent work, where the cell-surface interaction of *S. cerevisiae* was controlled by varying the ionic strength of the buffer solution (Yongabi et al., 2021). On the other hand, we kept such parameters the same for all samples to focus only on the geometry-dependent physical recognition in the current work.

The results from contact angle measurements indicate that the sensor

surface is hydrophilic, characterized by a water droplet contact angle of  $69.8^\circ$  (Fig. S4b, Supplementary Information). The total surface free energy and its polar and dispersive components were evaluated by measuring the surface tension using two different liquids: water and diiodomethane. The results indicate that the sensor surfaces have a moderate level of surface energy characterized by a total free energy of  $49.2$   $\text{mJ}/\text{m}^2$  (Fig. S4b table, Supplementary Information). It is difficult to comment the impact of this moderate level of surface wettability and surface free energy on *E. coli* attachment due to several conflicting findings in literature (Zheng et al., 2021). On the other hand, it is well known that having a SIP surface with moderate wettability mostly favors bacterial adhesion more than that of the surface with extreme contact angles (such as super-hydrophilic or super-hydrophobic surfaces) that can limit bacterial adhesion (Zheng et al., 2021; Yongabi et al., 2020). In addition, we suggest that the SIP layers can be stored for a long time as they underwent post-processing (flood exposure and post-bake) after their fabrication to ensure chemical stability, and they are not functionalized with biorecognition elements. Receptors, such as antibodies, can deteriorate over time in function of the environmental storage conditions.

Currently, a mass production and commercialization of the surface imprinted polymer-based bacteria detection sensors is the most important, but not yet achieved, goal in this field. In this work, we demonstrated that, once a functional master mold is created by photolithography, numerous replicas (positive master stamps) can easily be obtained from this mold by simple soft lithography without the need for photolithography again. Contrary to the conventional bacteria imprinting methods, during the chip fabrication, the areal density, depth, distribution, and orientation of the bacteria or bacterial imprints can be easily tuned without the need for a complex living component (bacteria). Therefore, this technology provides a mass-production-enabling approach.

### 3.2. Evaluation of *E. Coli* capturing

As it is obvious that more bacteria cells will be captured by a SIP-based sensor surface in comparison to a non-imprinted polymer (NIP)-based sensor surface, a higher sensitivity (lower detection limit) and selectivity should be achieved. Therefore, not only the cell-capturing ability of the *E. coli* SIP layer was tested, but also the contribution of specific pattern (cavity) geometries on this capturing ability was analyzed by comparing the *E. coli* SIP layer with the control SIP layer. Fig. 3 shows representative 3-D AFM topography images of two different types of SIP layers (*E. coli* SIP and control SIP) exposed to *E. coli* cells ( $10^8$  cells/mL in PBS) for 10 min. From the images, it can be seen that the number of captured *E. coli* cells on the surface of the *E. coli* SIP is higher than that of the control SIP. The images also indicate that the cells are mostly captured by the cavities rather than the flat non-patterned areas between the cavities. Surprisingly, captured cells on the control SIP layer are also located on - instead being inside of - the cavities, even if the geometry of the cavities does not match with the target bacteria: the cells on the control SIP layer appear to be protruding from the cavities rather than that of cells on the *E. coli* SIP, where the cells are mostly located inside the cavities.

To broaden the examination window and to get a better understanding of the surfaces’ capturing ability, SEM imaging was also performed. Fig. 4a and b demonstrate characteristic SEM images of the two different types of SIP layers (*E. coli* SIP and control SIP) exposed to *E. coli* cells ( $10^8$  cells/mL in PBS) for 20 min. The captured *E. coli* cells are marked with red ellipses on the images for better visualization (for the original images without red ellipses, see Fig. S5, Supplementary Information). In addition, SEM images for the captured cells after 10 min incubation with the cells are overviewed in Fig. S6 (Supplementary Information). As previously seen for the AFM images, the SEM images also indicate the superior *E. coli*-capturing ability of the *E. coli* SIP layer on the sensor surface. In addition, it was observed that the number of

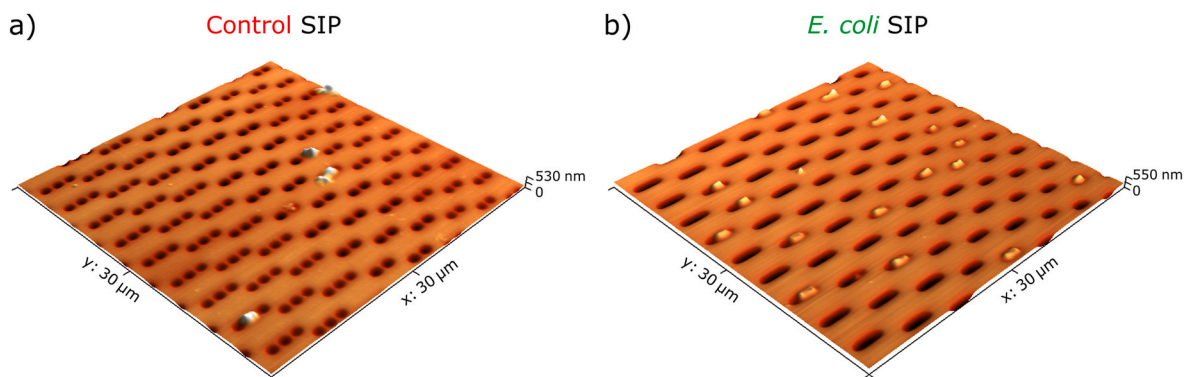


**Fig. 3.** Representative 3-D AFM height images show the captured *E. coli*-K12 cells on the sensor surfaces with a) control SIP (not matching with bacteria), and b) *E. coli* SIP (matching with bacteria). Note: the AFM imaging was performed after 10 min exposure with *E. coli* cells ( $10^8$  cells/mL in PBS). The surfaces were washed with PBS solution before fixing the remaining cells for AFM examinations.

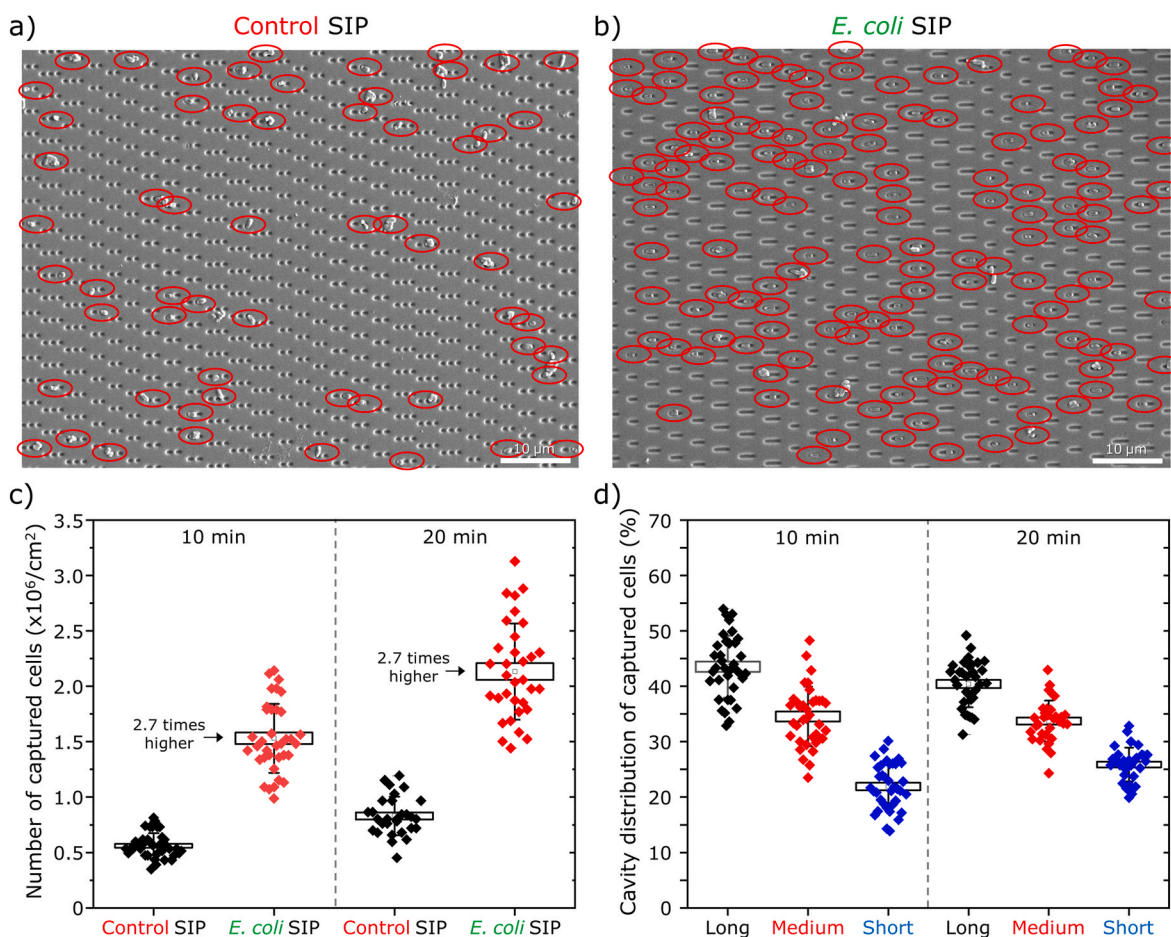


**Fig. 4.** Evaluation of *E. coli*-capturing ability of the different SIP layers on the sensor surface. a)-b) SEM images revealing the captured *E. coli*-K12 cells on the sensor surfaces with a) control SIP (control samples) and b) *E. coli* SIP. Note: SEM imaging was performed after 20 min exposure with *E. coli* cells ( $10^8$  cells/mL in PBS). The surfaces were washed with PBS solution before fixing the remaining cells for SEM experiments. The captured *E. coli* cells are highlighted with red ellipses on the images. c) Number of captured *E. coli*-K12 cells on the SIP surfaces after 10 min or 20 min exposure with cells ( $10^8$  cells/mL in PBS). Note: Cells captured inside the cavities including all different lengths were counted. d) Percentage of captured *E. coli*-K12 cells according to the length of the cavities (long: 2.6  $\mu\text{m}$ , medium: 2.1  $\mu\text{m}$ , short: 1.6  $\mu\text{m}$ ) on the sensor surface with *E. coli* SIP layers. Note: Each dot in the figures corresponds to the counting of cells captured in the cavities in each SEM image (a total number of  $n = 136$  SEM images was performed). The surfaces were washed with PBS buffer before fixing the remaining cells for SEM imaging.

captured cells inside the *E. coli* SIP cavities is higher than that of the flat, non-patterned area between the cavities. The difference in cell-capturing of imprinted (SIP or control SIP) and non-imprinted polymer (NIP)-based surfaces was also explored by SEM imaging from the border areas (intersection of imprinted and non-imprinted surfaces) on

the same sensor surfaces, see Fig. S7 (Supplementary Information).

A statistical evaluation of the cell-capturing efficiency of the different SIP layers was performed in order to conclude these findings. For this, a total number of 136 SEM images was recorded after incubating the *E. coli* cells on the surfaces for either 10 min or 20 min under

static conditions (no-flow). Each image was analyzed by counting the cells captured by the cavities using the ImageJ software (Schneider et al., 2012), and the “imprinting factor” (ratio between the number of *E. coli* cells bound on the SIP layer and cells bound on the control SIP) was calculated. The results are given in Fig. 4c. When the control SIP and *E. coli* SIP were compared after 10 min or 20 min long incubation with cells, the imprinting factor was around 2.7. In addition to counting the cells captured in the cavities (for the SIPs and control SIPs), the total number of cells that stayed adhered outside of the SIP cavities, that is the NIPs, was also counted. Related data is summarized in Fig. S8, (Supplementary Information). When the NIP samples and *E. coli* SIP samples were compared in terms of the total number of captured cells after 10 min incubation, the imprinting factor was found to be 2.2.

In a second bundle of the experiments we also checked the contribution of different cavity lengths on the *E. coli*-capturing ability. Fig. 4d shows the percentage of captured *E. coli*-K12 cells according to the length of the cavities (long: 2.6  $\mu\text{m}$ , medium: 2.1  $\mu\text{m}$ , short: 1.6  $\mu\text{m}$ ) on the sensor surface with *E. coli* SIP layers. The figure clearly indicates that the cells are more prone to being captured by long-length cavities as the highest percentage (43%) for 10 min incubation was observed in the long-length cavities. In contrast for medium-length and short-length cavities 35% and 22%, respectively, were found to be bound. Similarly, for 20 min incubation period, the highest percentage (40%) of trapped cells results for the long-length cavities. In contrast for medium-length and short-length cavities 34% and 26%, respectively, were found to be bound.

As one of the main findings in this work, the number of *E. coli* cells is statistically higher in the imprinted cavities, which have well-defined geometric features similar to rod-shaped bacteria, compared with non-imprinted (flat) surfaces or imprinted surfaces with non-matching geometric features. Traditionally, concluding the physicochemical mechanisms for this increased bacteria attachment is challenging due to their structural, chemical and biological complexity, superimposed with the complexity of the environmental features such as surface topography. Nevertheless, it is possible to comment on bacterial attachment characteristics in this study because, except for our test parameters (different surface topographies), all other conditions were kept constant during the experiments. Having higher cell capturing rate inside the *E. coli* cavities initially makes one think that the bacteria cells might better stay inside the cavities by escaping from fluid shear forces during washing steps as it is reported that shear forces outside of the cavities are usually higher than that inside (Chanasakulniyom et al., 2015; Tovar-Lopez et al., 2019). However, as observed on the control SIP surfaces with geometrically not perfectly matching cavities (Fig. 3 and 4a,b and Fig. S7), many of *E. coli* cells still stayed attached on those surfaces even if most of the cell bodies remained outside of the cavities (more protrusion-like effect).

Secondly, it is well documented that bacteria are capable of actively sensing and responding to surface mechanical cues, such as surface topography in particular, in which they regulate their attachment for different surface patterns (Cheng et al., 2019). For example, when the target bacteria are incubated on the surface, their appendages are shown to be consistently interacting with the surface, and they explore the surface topography and mediate their adhesion and attachment accordingly (Cheng et al., 2019; Friedlander et al., 2013). In addition, the rod-shaped *E. coli* cells in this study can orient themselves to meet the geometric constraints of the surface as well as to adapt to the thermodynamic requirements (Cheng et al., 2019). Most importantly, when topographic surface features (e.g., shape and size of the cavities) are in the same order of bacteria cells, it is considered a positive contributing factor for bacterial attachment inside those cavities: they strongly accommodate on the surface, take advantage of the maximized contact area ensuring better adhesion to it as well as properly shelter themselves inside the cavities (Lorenzetti et al., 2015; Helbig et al., 2016; Cheng et al., 2019; Filby et al., 2020; Zheng et al., 2021). Here, biomimetic structural analogues of real *E. coli* imprints might trigger such behavior.

The above-mentioned cell capturing mechanism based on the requirements of topography matching and maximized contact area could also help exclude specific adhesion of other bacteria smaller in size than *E. coli*. As an example from the traditional micro-contact imprinting method, a recent work (Stilman et al., 2022) reported that *S. aureus* bacteria - spherically shaped and smaller in size than *E. coli* - showed the lowest adhesion to *E. coli* cavities compared with other rod-shaped bacteria that have similar geometry with *E. coli*. On the other hand, it is quite difficult to solve the synergistic effect of both physical and chemical interactions causing low affinity to non-target bacteria in this work. In one study (Helbig et al., 2016) where the cavities were obtained by laser interference patterning (no imprinting), it was shown that a very low number of *S. epidermidis* cells - spherically shaped and smaller in size than *E. coli* - adhered on the larger cavities (around 5  $\mu\text{m}$  length) fabricated using an un-modified photoresist (SU-8) while a high number of *E. coli* cells adhered on these cavities. Furthermore, it is also worth mentioning that *E. coli* cells have inherently dynamic adhesion characteristics, evolving as a function of their growth phase, for instance, higher adhesion at the stationary phase than in the mid-log phase (Walker et al., 2005). Therefore, in addition to the late log (exponential) phase examined in this study, the adhesion behavior of the bacteria at different growth stages (especially, the stationary phase) should also be explored.

Although the importance of both chemical and physical recognition using bacteria-imprinted cavities has already been mentioned (Chen et al., 2016; Pan et al., 2018; Yongabi et al., 2018; Yadav et al., 2022; Caldara et al., 2023), to our best knowledge these findings are the first to specifically focus on the contribution of geometry-dependent physical recognition in SIP-based bacteria detection biosensors. The achieved results might form a basis for future studies dealing with not only molecular surface imprinted polymer-based whole bacteria sensors but also other technologies aiming for the direct detection of whole bacteria. For example, such engineered biomimetic cavities can be incorporated with other biorecognition elements (e.g., aptamers and antibodies) to enhance the sensing performance. On the other hand, further research is needed to explore the full potential of the method, especially by developing new biomimetic imprints for different bacteria species and strains, and demonstrating their applicability under different conditions. In addition, the current study did not demonstrate the cross-selectivity of the developed SIP layer by testing different bacteria species, in particular, whose shape and size are similar to rod-shaped *E. coli* cells. Highly selective sensing (even for distinguishing the different strains of the same species) requires chemical recognition inside the cavities that is normally provided by outer membrane components of the template bacteria, which leave their imprints inside the cavities during the conventional micro-contact imprinting method. For this, our on-going work is focusing on the functionalization of the stamp surface with outer membrane components of the target bacteria (e.g., lipopolysaccharides isolated from *E. coli* cells) to add a selective detection ability based on chemical recognition.

### 3.3. Binding-signal measurements

As it is demonstrated in the previous section, the sensor chips with *E. coli* SIP layer can capture the target bacteria cells (*E. coli*-K12) from the analyte solution. In this section, the feasibility of signal measurements (impedance spectroscopy and QCM) to detect the target bacteria by employing *E. coli* SIP-based sensor chips was explored. Therefore, signal measurements were performed using the two different types of sensors (see Section 2.7) with photopolymer resin-based SIP layers.

Fig. 5 shows Nyquist plots of electrochemical impedance spectroscopy using *E. coli* SIP-covered sensor chips with interdigitated electrodes. The red curve (with dots) represents the plot after measurement with PBS solution (without cells). After 20 min-long cell ( $10^8$  cells/mL in PBS) exposure and properly washing with PBS solution, the curve was shifted towards higher impedance values (the green curve with triangle

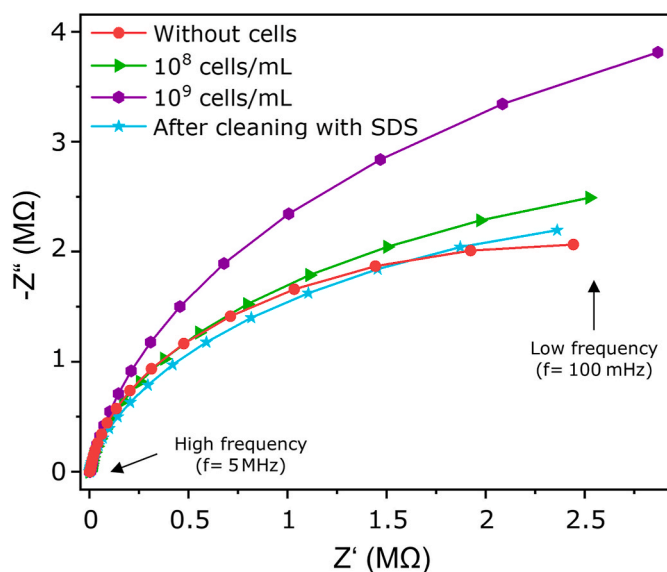


**Fig. 5.** Nyquist plot of electrochemical impedance spectroscopy with *E. coli*-K12 cells using an interdigitated electrode-based sensor with *E. coli* SIP layer. Each measurement was performed after washing the sensor surface in the fluidic channel with PBS solution following a 20 min-long cell exposure. For measurements, 10 mM  $\text{Fe}(\text{CN})_6^{3-}/\text{Fe}(\text{CN})_6^{4-}$  is used as a redox probe. 2% of sodium dodecyl sulfate solution was used for detaching the captured cells to evaluate the recovery of the impedance signal.

symbols). Further incubation with the cells in a higher concentration ( $10^9$  cells/mL in PBS) caused the curve shift more to increasing impedance values (purple line with hexagon symbols). These signal changes can be explained by the alteration in capacitive and resistive behavior of the sensor chip corresponding to the bound *E. coli* cells. To verify that the signal response arises from capturing the cells and not due to the impact of other external factors, the impedance measurement was repeated after thoroughly cleaning the channels of the measurement cell: the sensor chip surface was exposed to a detergent solution (2% SDS in ultrapure water) to remove all captured cells from the SIP layer. This results in a signal recovery (see cyan line with star-shaped symbols) as the plot almost approached its initial values, where measurements were performed without employing the *E. coli* cells. The experiments could successfully indicate that the sensor chip with *E. coli* SIP layer responds to the binding of cells at different concentrations with different signal amplitudes.

It is also worth mentioning that the impedance signal response for cell concentrations below  $10^8$  cells/mL was hardly detectable. This could be due to the low-conductive nature and poor capacitive properties of the imprinted polymer layer used in this experiment, which can be seen from the high impedance characteristics of the developed SIP film (Fig. 5). Such phenomenon has previously been discussed in the literature (Stilman et al., 2021; Feldner et al., 2023; Lazanas and Prodromidis, 2023). In the current study, the thickness of the fabricated SIP layer on the interdigitated electrodes (IDEs) is 600 nm, and the depth of the cavities is around 530 nm (Fig. 2). This means that there is still a residual polymer layer (with a thickness of around 70 nm) left between the cavities and the IDEs, which could cause a high electrical resistance, correspondingly resulting in a decreased measurement sensitivity compared to reports in literature, where higher sensitivity values (lower detection limits) were achieved using traditional SIP-based detection methods (Cornelis et al., 2019; Stilman et al., 2022). Therefore, in future experiments we plan to explore potential applicabilities of conductive polymers for our imprinting concept as well as an optimization of the imprinting parameters to decrease the thickness of the undesired residual polymer layer (Bossi et al., 2001).

It is important to evaluate the suitability of a novel sensing strategy

for different sensing platforms to explore its versatility. Therefore, in addition to the impedance-based platform, the developed sensing strategy based on the *E. coli* SIP layer was tested with a quartz crystal microbalance with dissipation monitoring technique (QCM-D). Fig. 6a shows the responses of the QCM sensor chip coated with an *E. coli* SIP layer to monitor the capturing of *E. coli*-K12 cells. After the initial measurements with PBS solution as baseline signal, *E. coli*-K12 cells in different concentrations (from  $10^4$  cells/mL to  $10^9$  cells/mL in PBS) were injected into the microfluidic-based flow cell of the device where the sensor chip was located. As a typical response behavior of frequency change ( $\Delta f_n/n$ , where “n” indicates the overtone number), when the cells are exposed to the sensor surface, a decrease in the frequency is observed. The change in frequency is usually related to the change in mass ( $\Delta m$ ), hence the amount of the target cells interacting with the surface (Dixon, 2008; Alexander et al., 2019). The frequency changes were more pronounced after applying the cells in higher concentrations such as  $10^7$  cells/mL,  $10^8$  cells/mL, and  $10^9$  cells/mL. All six overtones ( $n = 3, 5, 7, 9, 11, 13$ ) followed the same trend, and the raw data with other overtones were given in the inset of Fig. S9 (Supplementary Information).

In addition, from Fig. 6a, the washing steps in between the cell exposures did not result in a substantial influence on the QCM signal. This could indicate that the sensor signal is mostly related to the *E. coli* cells attached on the *E. coli* SIP layer. To further validate the signal changes due to the impact of the cells, the sensor chip surface was cleaned with a detergent solution (2% SDS in ultrapure water) to remove the captured bacteria from the SIP layer at the end of the measurement. As indicated in Fig. 6a (towards the end of the measurements), this cleaning step caused an almost perfect signal recovery as the plot approached its initial value, where the measurement started without employing the cells. Considering the total operational measurement time of the sensor chip (longer than 12 h in this experiment) without any signal disturbances, it might be concluded that the sensor delivers stable signal measurements over a number of bacteria exposure and rinsing steps. In addition, the high signal recovery observed after cleaning the chip surface with SDS solution suggests an efficient washing out of the template bacteria from the cavities, which is also important to achieve reusability of the sensor chip. Furthermore, to explore the stability of the fabricated SIP layer and to check whether there is any long-term structural degradation, damage, or delamination, the chip was incubated in sterile PBS buffer at room temperature (21 °C) for 72 h after recording its digital microscopy images. The imaging was repeated every 24 h. Fig. S10 (Supplementary Information) shows that this long-term incubation procedure with PBS buffer did not negatively influence the structural integrity of the SIP layer. On the other hand, further research is needed to fully understand other characteristic sensor-performance criteria (e.g., service life, drift, selectivity, accuracy). The findings indicate that the QCM sensor chip with an *E. coli* SIP layer reliably responds to the application of *E. coli* cells in different concentrations. As mentioned above, future optimization of the SIP layer properties, such as layer thickness and areal density of the cavities, could further improve the QCM sensor signal response. In addition, due to the damping effect, instead of viscoelastic SIP layers, more rigid (glassy) materials might be employed as SIP layers, offering an alternative strategy in enhancing the sensor characteristics (Hayden et al., 2006b, 2006a; Latif et al., 2014; Easley et al., 2022).

Dissipation monitoring is another way to evaluate the adhesion process of the *E. coli* cells. Fig. 6b shows results from quartz crystal microbalance with dissipation monitoring (QCM-D). As typical response behavior of dissipation change ( $\Delta D$ ), when the *E. coli* cells were bound to the sensor surface, an increase in dissipation is observed corresponding to the amount of *E. coli* cells interacting with the sensor surface. The dissipation change was more pronounced when using the cells in higher concentrations such as  $10^7$ ,  $10^8$ , and  $10^9$  cells/mL. From these results, it can be concluded that similar to the results from impedance spectroscopy, the limit of detection (LoD) of the *E. coli* SIP-based QCM-D sensor

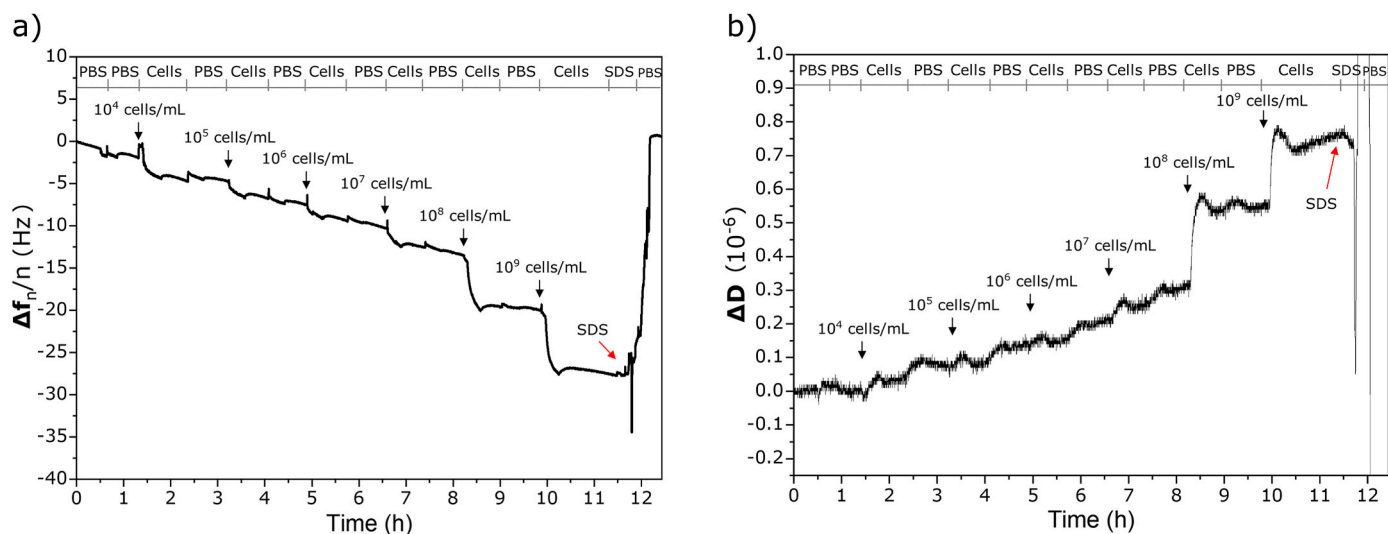


**Fig. 6.** a) Quartz crystal microbalance (QCM) and b) quartz crystal microbalance with dissipation (QCM-D) sensor signals for monitoring the captured *E. coli*-K12 cells with *E. coli* SIP layer on the sensor surface. The cells for each concentration were introduced to the sensor surface by the microfluidic set-up of the QCM device for 20 min with a flow rate of 100  $\mu\text{L}/\text{min}$ , and then, the measurement was continued under static conditions (no-flow) for 30 min. Afterwards, the same procedure was applied with PBS solution (no cells) to wash the surface with a flow rate of 50  $\mu\text{L}/\text{min}$ . 2% of sodium dodecyl sulfate (SDS) solution was used for detaching the captured cells to evaluate the signal recovery. “n”, overtone number; “D”, dissipation. Note: The graphs in the figures show overtone  $n = 9$ .

chip is around  $10^7$  cells/mL with a detection range of  $10^7$  to  $10^9$  cells/mL. The LoD and sensitivity we achieved can find application in, for example, sensors for bioreactors, in which generally high *E. coli* concentrations are cultivated (Glazyrina et al., 2010; Samardzic et al., 2014). The change in dissipation is usually related to the change in surface viscoelastic properties (Alexander et al., 2019; Dixon, 2008). The measurements allow probing the energetic losses in the form of dissipation due to the contribution of viscous and elastic components of the captured cell (Alexander et al., 2019; Dixon, 2008). On the other hand, compared with the only frequency-based QCM measurement (Fig. 6a), QCM-D results seem superior in terms of studying the drift behavior that can be seen on the first measurement period of the figure, where the initial measurements have been performed with PBS solution for baseline signal observation. This might be due to one of the benefits of the QCM-D technique, where it can be used to reliably monitor viscoelastic materials (such as cells in contact with liquid) instead of rigid materials, in which the frequency-based QCM technique performs better (Easley et al., 2022). Together, these findings indicate that sensor chips, synthesized with the as-described method, can serve for the quantitative detection of *E. coli* bacteria. To function then in a reliable way, still a variety of aspects need to be studied and documented, including the dose-response calibration curve, the reusability and the stability under long-term storage.

#### 4. Conclusion

Surface imprinted polymer (SIP)-based biosensors with biomimetic *E. coli* imprints ( $10^7$  cavities per  $\text{cm}^2$ ) were achieved by micro-contact imprinting method using a PDMS-based positive master stamp containing photolithographic mimics of *E. coli* cells. These structural analogues of conventional *E. coli* imprints (cavities) were patterned onto the sensor chip surface in a high areal density, desired distribution and orientation without the need for real template bacteria. The presence of biomimetic cavities increases the *E. coli*-capturing ability of the SIP layer on the sensor surface, especially the cavities with a specific length play an important role in the *E. coli* attachment inside. *E. coli* detection feasibility of the biomimetic SIP-based interdigitated electrodes and QCM chips was demonstrated using two different sensing methods: electrochemical impedance spectroscopy and quartz crystal microbalance with dissipation monitoring technique.

This study emphasises on the contribution of geometry-dependent physical recognition in SIP-based bacteria detection biosensors. The key contribution of this work highlights a first step towards “template bacteria-free” and “reproducible” fabrication of SIP layers. However, as a necessity, this new imprinting technology should further be improved by coating the stamp surface with outer membrane components of the target bacteria of interest (e.g., lipopolysaccharides isolated from the target bacteria) to facilitate selective detection based on chemical recognition. In addition, the full potential of this technology should be explored by addressing one of the most important challenges arising from the low-conductive nature and poor capacitive properties of conventional surface imprinting polymers such as photopolymers and polyurethane. Therefore, our group currently focuses on advancing this biomimetic imprinting concept by employing conductive polymers such as poly(3,4-ethylenedioxythiophene)-poly(styrenesulfonate) (PEDOT:PSS) and conductive fillers (e.g., nanoparticles) as well as their blends with functional monomers.

#### CRedit authorship contribution statement

**Dua Özsoylu:** Writing – review & editing, Writing – original draft, Methodology, Investigation, Formal analysis, Conceptualization. **Fereshteh Aliazizi:** Investigation. **Patrick Wagner:** Writing – review & editing, Validation, Supervision. **Michael J. Schöning:** Writing – review & editing, Writing – original draft, Validation, Supervision, Funding acquisition, Conceptualization.

#### Declaration of competing interest

The authors declare that they have no known competing financial interests or personal relationships that could have appeared to influence the work reported in this paper.

#### Data availability

Data will be made available on request.

#### Acknowledgements

The authors would like to thank the European Commission and the

German Federal Ministry of Education and Research (project no.: 03F0902A) for funding in the frame of the collaborative international consortium (ARENA) financed under the 2020 AquaticPollutants Joint call of the AquaticPollutants ERA-NET Cofund (N° 869178). Furthermore, the authors would like to thank H. Iken for the support for the fabrication of interdigitated electrodes, E. Börmann-El Kholy for the help at bacteria cultivation, D. Rolka for the support in SEM image analysis, R. Shahi, E. Özler and H. Aboelmagd for their help for counting the cells, and M. Khorshid and S. Bakhshi Sichani for the support during QCM measurements.

## Appendix A. Supplementary data

Supplementary data to this article can be found online at <https://doi.org/10.1016/j.bios.2024.116491>.

## References

- Abayasekara, L.M., Perera, J., Chandrasekharan, V., Gnanam, V.S., Udunuwara, N.A., Liyanage, D.S., Bulathsinhala, N.E., Adikary, S., Aluthmuhandiram, J.V.S., Thanaseelan, C.S., Tharmakulasingam, D.P., Karunakaran, T., Ilango, J., 2017. *BMC Infect. Dis.* 17, 631. <https://doi.org/10.1186/s12879-017-2727-8>.
- Alexander, T.E., Lozeau, L.D., Comesano, T.A., 2019. *The Cell Surface* 5, 100024. <https://doi.org/10.1016/j.tcs.2019.100024>.
- Arreguin-Campos, R., Eersels, K., Lowdon, J.W., Rogosic, R., Heidt, B., Caldara, M., Jiménez-Monroy, K.L., Diliën, H., Cleij, T.J., van Grinsven, B., 2021. *Microchem. J.* 169, 106554. <https://doi.org/10.1016/j.microc.2021.106554>.
- Arreguin-Campos, R., Eersels, K., Rogosic, R., Cleij, T.J., Diliën, H., van Grinsven, B., 2022. *ACS Sens.* 7, 1467–1475. <https://doi.org/10.1021/acssens.2c00215>.
- Bossi, A., Piletsky, S.A., Piletska, E.V., Righetti, P.G., Turner, A.P.F., 2001. *Anal. Chem.* 73, 5281–5286. <https://doi.org/10.1021/ac0006526>.
- Caldara, M., van Wissen, G., Cleij, T.J., Diliën, H., van Grinsven, B., Eersels, K., Lowdon, J.W., 2023. *Advanced Sensor Research* 2, 1–18. <https://doi.org/10.1002/adr.202200059>.
- Castle, L.M., Schuh, D.A., Reynolds, E.E., Furst, A.L., 2021. *ACS Sens.* 6, 1717–1730. <https://doi.org/10.1021/acssens.1c00481>.
- Chanasakulniyom, M., Glidle, A., Cooper, J.M., 2015. *Lab Chip* 15, 208–215. <https://doi.org/10.1039/C4LC00774C>.
- Chen, L., Wang, X., Lu, W., Wu, X., Li, J., 2016. *Chem. Soc. Rev.* 45, 2137–2211. <https://doi.org/10.1039/C6CS00061D>.
- Cheng, Y., Feng, G., Moraru, C.I., 2019. *Front. Microbiol.* 10, 1–17. <https://doi.org/10.3389/fmicb.2019.00191>.
- Cornelis, P., Givanoudi, S., Yongabi, D., Iken, H., Duwé, S., Deschaume, O., Robbens, J., Dedeker, P., Bartic, C., Wübbenhorst, M., Schöning, M.J., Heyndrickx, M., Wagner, P., 2019. *Biosens. Bioelectron.* 136, 97–105. <https://doi.org/10.1016/j.bios.2019.04.026>.
- Dixon, M.C., 2008. *J. Biomol. Tech.: J. Biochem. (Tokyo)* 19, 151–158.
- Easley, A.D., Ma, T., Eneh, C.I., Yun, J., Thakur, R.M., Lutkenhaus, J.L., 2022. *J. Polym. Sci.* 60, 1090–1107. <https://doi.org/10.1002/pol.20210324>.
- Eersels, K., Lieberzeit, P., Wagner, P., 2016. *ACS Sens.* 1, 1171–1187. <https://doi.org/10.1021/acssens.6b00572>.
- Feldner, A., Völkle, J., Lieberzeit, P., Fruhmann, P., 2023. *Chemosensors* 11, 299. <https://doi.org/10.3390/chemosensors11050299>.
- Filby, B.W., Hardman, M.J., Paunov, V.N., 2020. *Nano Select* 1, 673–688. <https://doi.org/10.1002/nano.202000113>.
- Friedlander, R.S., Vlamakis, H., Kim, P., Khan, M., Kolter, R., Aizenberg, J., 2013. *Proc. Natl. Acad. Sci. USA* 110, 5624–5629. <https://doi.org/10.1073/pnas.1219662110>.
- Givanoudi, S., Cornelis, P., Rasschaert, G., Wackers, G., Iken, H., Rolka, D., Yongabi, D., Robbens, J., Schöning, M.J., Heyndrickx, M., Wagner, P., 2021. *Sensor. Actuator. B Chem.* 332, 129484. <https://doi.org/10.1016/j.snb.2021.129484>.
- Glazyrina, J., Materne, E.M., Dreher, T., Storm, D., Junne, S., Adams, T., Greller, G., Neubauer, P., 2010. *Microb. Cell Factories* 9, 42. <https://doi.org/10.1186/1475-2859-9-42>.
- Golabi, M., Kuralay, F., Jager, E.W., Beni, V., Turner, A.P., 2017. *Biosens. Bioelectron.* 93, 87–93. <https://doi.org/10.1016/j.bios.2016.09.088>.
- Hayden, O., Lieberzeit, P.A., Blaas, D., Dickert, F.L., 2006a. *Adv. Funct. Mater.* 16, 1269–1278. <https://doi.org/10.1002/adfm.200500626>.
- Hayden, O., Mann, K., Krassnig, S., Dickert, F.L., 2006b. *Angew. Chem. Int. Ed.* 45, 2626–2629. <https://doi.org/10.1002/anie.200502857>.
- Helbig, R., Günther, D., Friedrichs, J., Röller, F., Lasagni, A., Werner, C., 2016. *Biomater. Sci.* 4, 1074–1078. <https://doi.org/10.1039/C6BM00078A>.
- Iakimova, T.M., Heidt, B., Shen, A.Q., 2024. *Cell Reports Physical Science*, 101853. <https://doi.org/10.1016/j.xcrp.2024.101853> (in press).
- Idil, N., Bakhshpour, M., Percin, I., Mattiasson, B., 2021. *Biosensors* 11, 140. <https://doi.org/10.3390/bios11050140>.
- Idil, N., Hedström, M., Denizli, A., Mattiasson, B., 2017. *Biosens. Bioelectron.* 87, 807–815. <https://doi.org/10.1016/j.bios.2016.08.096>.
- Jamal, R.B., Shipovskov, S., Ferapontova, E.E., 2020. *Sensors* 20, 5561. <https://doi.org/10.3390/s20195561>.
- Kavand, H., van Lintel, H., Bakhshi Sichani, S., Bonakdar, S., Kavand, H., Koohsorkhi, J., Renaud, P., 2019. *ACS Appl. Mater. Interfaces* 11, 10559–10566. <https://doi.org/10.1021/acsami.9b00523>.
- Latif, U., Qian, J., Can, S., Dickert, F., 2014. *Sensors* 14, 23419–23438. <https://doi.org/10.3390/s141223419>.
- Law, J.W.F., Ab Mutalib, N.S., Chan, K.G., Lee, L.H., 2015. *Front. Microbiol.* 5, 1–19. <https://doi.org/10.3389/fmicb.2014.00770>.
- Lazanas, A.C., Prodromidis, M.I., 2023. *ACS Measurement Science* Au 3, 162–193. <https://doi.org/10.1021/acsmes.2c00070>.
- Li, J., McLandsborough, L., 1999. *Int. J. Food Microbiol.* 53, 185–193. [https://doi.org/10.1016/S0168-1605\(99\)00159-2](https://doi.org/10.1016/S0168-1605(99)00159-2).
- Lorenzetti, M., Dogša, I., Stošić, T., Stopar, D., Kalin, M., Kobe, S., Novak, S., 2015. *ACS Appl. Mater. Interfaces* 7, 1644–1651. <https://doi.org/10.1021/am507148n>.
- Mazur, F., Tjandra, A.D., Zhou, Y., Gao, Y., Chandrawati, R., 2023. *Nature Reviews Bioengineering* 1, 180–192. <https://doi.org/10.1038/s44222-023-00024-w>.
- Owens, D.K., Wendt, R.C., 1969. *J. Appl. Polym. Sci.* 13, 1741–1747. <https://doi.org/10.1002/app.1969.070130815>.
- Pahlow, S., Meisel, S., Cialla-May, D., Weber, K., Rösch, P., Popp, J., 2015. *Adv. Drug Deliv. Rev.* 89, 105–120. <https://doi.org/10.1016/j.addr.2015.04.006>.
- Pan, J., Chen, W., Ma, Y., Pan, G., 2018. *Chem. Soc. Rev.* 47, 5574–5587. <https://doi.org/10.1039/C7CS00854F>.
- Park, K.S., 2018. *Biosens. Bioelectron.* 102, 179–188. <https://doi.org/10.1016/j.bios.2017.11.028>.
- Piletsky, S., Canfarotta, F., Poma, A., Bossi, A.M., Piletsky, S., 2020. *Trends Biotechnol.* 38, 368–387. <https://doi.org/10.1016/j.tibtech.2019.10.002>.
- Poller, A.M., Spieker, E., Lieberzeit, P.A., Preininger, C., 2017. *ACS Appl. Mater. Interfaces* 9, 1129–1135. <https://doi.org/10.1021/acsami.6b13888>.
- Reshes, G., Vanounou, S., Fishov, I., Feingold, M., 2008. *Biophys. J.* 94, 251–264. <https://doi.org/10.1529/biophysj.107.104398>.
- Samardzic, R., Sussitz, H.F., Jongkon, N., Lieberzeit, P.A., 2014. *Sens. Lett.* 12, 1152–1155. <https://doi.org/10.1166/sl.2014.3201>.
- Schneider, C.A., Rasband, W.S., Eliceiri, K.W., 2012. *Nat. Methods* 9, 671–675. <https://doi.org/10.1038/nmeth.2089>.
- Steen Redeker, E., Eersels, K., Akkermans, O., Royakkers, J., Dyson, S., Nurekeyeva, K., Ferrando, B., Cornelis, P., Peeters, M., Wagner, P., Diliën, H., van Grinsven, B., Cleij, T.J., 2017. *ACS Infect. Dis.* 3, 388–397. <https://doi.org/10.1021/acinfecdis.7b00037>.
- Stilman, W., Campolim Lenzi, M., Wackers, G., Deschaume, O., Yongabi, D., Mathijssen, G., Bartic, C., Gruber, J., Wübbenhorst, M., Heyndrickx, M., Wagner, P., 2022. *Phys. Status Solidi* 219, 1–13. <https://doi.org/10.1002/pssa.202100405>.
- Stilman, W., Yongabi, D., Bakhshi Sichani, S., Thesseling, F., Deschaume, O., Putzeys, T., Pinto, T.C., Verstrepen, K., Bartic, C., Wübbenhorst, M., Heyndrickx, M., Wagner, P., 2021. *Sensor. Actuator. B Chem.* 340, 129917. <https://doi.org/10.1016/j.snb.2021.129917>.
- Tovar-Lopez, F., Thurgood, P., Gilliam, C., Nguyen, N., Pirogova, E., Khoshmanesh, K., Baratchi, S., 2019. *Front. Bioeng. Biotechnol.* 7, 1–7. <https://doi.org/10.3389/fbioe.2019.00081>.
- Uzun, L., Turner, A.P., 2016. *Biosens. Bioelectron.* 76, 131–144. <https://doi.org/10.1016/j.bios.2015.07.013>.
- Velican, A.M., Măruțescu, L., Kamerzan, C., Cristea, V.C., Banu, O., Borcan, E., Chifriuc, M.C., 2020. *Microorganisms* 8, 1233. <https://doi.org/10.3390/microorganisms8081233>.
- Walker, S.L., Hill, J.E., Redman, J.A., Elimelech, M., 2005. *Appl. Environ. Microbiol.* 71, 3093–3099. <https://doi.org/10.1128/AEM.71.6.3093-3099.2005>.
- Werner, M., Glück, M.S., Bräuer, B., Bismarck, A., Lieberzeit, P.A., 2022. *Soft Matter* 18, 2245–2251. <https://doi.org/10.1039/D2SM00137C>.
- World Health Organization, 2015. WHO estimates of the global burden of food-borne diseases. URL: [https://iris.who.int/bitstream/handle/10665/199350/9789241565165\\_eng.pdf?sequence=1](https://iris.who.int/bitstream/handle/10665/199350/9789241565165_eng.pdf?sequence=1).
- World Health Organization, 2022. Food safety. URL: <https://www.who.int/NEWS-ROOM/FACT-SHEETS/DETAIL/FOOD-SAFETY>.
- Yadav, A.K., Verma, D., Dalal, N., Kumar, A., Solanki, P.R., 2022. *Biosens. Bioelectron. X* 12, 100257. <https://doi.org/10.1016/j.biox.2022.100257>.
- Yang, Q., Li, J., Wang, X., Peng, H., Xiong, H., Chen, L., 2018. *Biosens. Bioelectron.* 112, 54–71. <https://doi.org/10.1016/j.bios.2018.04.028>.
- Yilmaz, E., Majidi, D., Ozgur, E., Denizli, A., 2015. *Sensor. Actuator. B Chem.* 209, 714–721. <https://doi.org/10.1016/j.snb.2014.12.032>.
- Yongabi, D., Jooen, S., Givanoudi, S., Khorshid, M., Deschaume, O., Bartic, C., Losada-Pérez, P., Wübbenhorst, M., Wagner, P., 2021. *J. Colloid Interface Sci.* 585, 583–595. <https://doi.org/10.1016/j.jcis.2020.10.038>.
- Yongabi, D., Khorshid, M., Gennaro, A., Jooen, S., Duwé, S., Deschaume, O., Losada-Pérez, P., Dedeker, P., Bartic, C., Wübbenhorst, M., Wagner, P., 2020. *ACS Appl. Mater. Interfaces* 12, 18258–18272. <https://doi.org/10.1021/acsami.0c00353>.
- Yongabi, D., Khorshid, M., Losada-Pérez, P., Eersels, K., Deschaume, O., D'Haen, J., Bartic, C., Hooyberghs, J., Thoelen, R., Wübbenhorst, M., Wagner, P., 2018. *Sensor. Actuator. B Chem.* 255, 907–917. <https://doi.org/10.1016/j.snb.2017.08.122>.
- Zaraee, N., Kanik, F.E., Bhuiya, A.M., Gong, E.S., Geib, M.T., Lortlar Ünlü, N., Ozkumur, A.Y., Dupuis, J.R., Ünlü, M.S., 2020. *Biosens. Bioelectron.* 162, 112258. <https://doi.org/10.1016/j.bios.2020.112258>.
- Zhao, Y., Zeng, D., Yan, C., Chen, W., Ren, J., Jiang, Y., Jiang, L., Xue, F., Ji, D., Tang, F., Zhou, M., Dai, J., 2020. *The Analyst* 145, 3106–3115. <https://doi.org/10.1039/D0AN00224K>.
- Zheng, S., Bawazir, M., Dhall, A., Kim, H.E., He, L., Heo, J., Hwang, G., 2021. *Front. Bioeng. Biotechnol.* 9, 1–22. <https://doi.org/10.3389/fbioe.2021.643722>.